Inorg. Chem. **2008**, *47*, 11633−11643

Mixed Valence Creutz−Taube Ion Analogues Incorporating Thiacrowns: Synthesis, Structure, Physical Properties, and Computational Studies

Harry Adams,[†] Paulo J. Costa,[‡] Mike Newell,[†] Steven J. Vickers,[†] Michael D. Ward,[†] Vítor Félix,*[,‡] and Jim A. Thomas*[,†]

Department of Chemistry, University of Sheffield, Sheffield S3 7HF, U.K., and Departamento de Química, CICECO and Secção Autónoma de Ciências da Saúde, Universidade de Aveiro, 3810-193 Aveiro, Portugal

Received June 27, 2008

A series of nine new complexes incorporating $[Ru^{II}Cl([n]aneS_3)]$ (n = 12, 14, 16) metal centers bridged by three ditopic ligands containing two monodentate sites (pyrazine, 4,4′-bipyridine, and 3,6-bis(4-pyridyl)-1,2,4,5-tetrazine) have been synthesized and fully characterized. The solid-state structures of three of the complexes have been further characterized by X-ray crystallography studies. Intermetallic interactions within the new systems have been probed using electrochemistry and optical spectroscopy. Cyclic voltammetry reveals that the three pyrazine bridged systems display two separate $Ru^{III/II}$ redox couples. Using spectroelectrochemistry, we have investigated the optical properties of these mixed valence, Creutz−Taube ion analogues. An analysis of the intervalence charge transfer bands for the complexes revealed that, despite possessing the same donor sets, the electronic delocalization within these systems is modulated by the nature of the coordinated thiacrown. Computational modeling using density function theory offers further evidence of interaction between metal centers and provides insights into how these interactions are mediated.

Introduction

The Creutz−Taube (CT) ion $[(NH_3)_5Ru(\mu\text{-pyz})Ru(NH_3)_5]^{5+}$(where pyz = pyrazine) is the archetypical $Ru^{III/II}$ mixed valence (MV) system; since it was first synthesized almost forty years ago[1] it has been the focus of numerous studies, all aimed at determining the extent of intermetallic electron delocalization. By the end of the past decade, the weight of evidence indicated that the complex was a Robin and Day Class III,[2] valence delocalized, system.[3] However, more recently, it has been suggested that its properties are more appropriately described as a Class II/III, solvent averaged, valence localized system.[4]

Within the context of molecular electronics and nanotechnology,[5] MV systems are of interest as they could form the basis of devices such as wires and switches; furthermore, their study addresses many fundamental questions concerning electron transfer, a phenomenon that underpins many biological processes.[6] Consequently, numerous CT-ion analogues have been reported.[7] However, while many different bridging ligands have been employed, the vast majority of these systems involve very similar metal-centers based on common N-donor ligands such as NH_3 and 2,2′-bipyridine. Given that many biological ET systems are based on transition metals coordinated to sulfur donor sites, we have

* To whom correspondence should be addressed. E-mail: vitor.felix@ua.pt (V.F.), james.thomas@sheffield.ac.uk (J.A.T.).
† University of Sheffield.
‡ Universidade de Aveiro.

(1) (a) Creutz, C.; Taube, H. *J. Am. Chem. Soc.* **1969**, *91*, 3988. (b) Creutz, C.; Taube, H. *J. Am. Chem. Soc.* **1973**, *95*, 1086.
(2) Robin, M. B.; Day, P. *Adv. Inorg. Chem. Radiochem.* **1967**, *10*, 247.
(3) (a) Oh, D.; Sano, M.; Boxer, S. G. *J. Am. Chem. Soc.* **1991**, *113*, 6880. (b) Crutchley, R. J. *Adv. Inorg. Chem.* **1994**, *41*, 273. (c) Bencini, A.; Ciofini, I.; Daul, C. A.; Feretti, A. *J. Am. Chem. Soc.* **1999**, *121*, 11418.
(4) (a) Demadis, K. D.; Hartshorn, C. M.; Meyer, T. J. *Chem. Rev.* **2001**, *101*, 2655. (b) Brunschwig, B. S.; Creutz, C.; Sutin, N. *Chem. Soc. Rev.* **2002**, *31*, 168. (c) D'Alessandro, D. M.; Keene, F. R. *Chem. Soc. Rev.* **2006**, *35*, 424. (d) D'Alessandro, D. M.; Topley, A. C.; Davies, M. S.; Keene, F. R. *Chem.—Eur. J.* **2006**, *12*, 4873.
(5) (a) Ward, M. D. *Chem. Soc. Rev.* **1995**, *24*, 121. (b) *Molecular Electronics*; Jortner, J., Ratner. M., Eds.; Blackwell Science: Cambridge, MA, 1997. (c) Paul, F.; Lapinte, C. *Coord. Chem. Rev.* **1998**, *178−180*, 431. (d) *Nanotechnology Research Direction - Visions for Nanotechnology R&D in the Next Decade*; Roco, M. C., Williams, R. S., Alivistos, P., Eds.; Kluwer: Norwell, MA, 2000. (e) Joachim, C.; Gimzewski, J. K.; Aviram, A. *Nature* **2000**, *408*, 541. (f) *Molecular Switches*, Feringa, B. L., Ed.; Wiley-VCH: New York, 2001. (g) Carrroll, R. L.; Gorman, C. B. *Angew, Chem, Int. Ed.* **2002**, *41*, 4378. (h) Robeertson, N.; McGowan, C. A. *Chem. Soc. Rev.* **2003**, *32*, 96. (i) Wolf, E. D. *Nanophysics and Nanotecnology*, 2nd ed.; Wiley-VCH: New York, 2006.

10.1021/ic801193r CCC: $40.75
Published on Web 11/14/2008

been investigating how the incorporation of sulfur donating thiacrown ligands modulate the ET properties of MV complexes. Our initial reports concerned dinuclear complexes containing $[RuCl([9]aneS_3)]^+$ metal centers bridged by ligands containing two bidentate sites, such as 2,3-bis(2-pyridyl)pyrazine, and 3,6-bis(2-pyridyl)-1,2,4,5- tetrazine.[8] This work led to complexes that displayed intense intermetallic coupling, with interactions that were at least as high as those in any conventional N-donor system. An extension of this work led to the synthesis of redox active trinuclear metallomacrocycles with more than one MV state.[9,10]

In more recent work, using the same ligands, we extended these studies to $[Ru([n]aneS_4)]^{2+}$ based systems (where n = 12, 14, and 16).[11,12] In these complexes it was found that oxidation of the Ru^{II} centers is considerably anodically shifted and interactions between metal centers in the MV states is less intense than that of their $[RuCl([9]aneS_3)]^+$ analogues. This was because the substitution of the π-donor chloride ligand of the S_3 systems with an electron-accepting macrocyclic sulfur ligand[11,12] results in a decrease of electron density on the metal center, thus stabilizing the Ru^{II} oxidation state and lowering the electron density available for delocalization over the bridging ligand. Furthermore, it was found that the intensity of the electrochemical and electronic interactions was modulated by the nature of the coordinated $[n]aneS_4$, due to the differing coordination preferences of each thiacrown ligand and the consequent changes in orbital overlap between the metal centers and bridging ligands.

With the aim of broadening these studies and creating systems that can be more easily compared to the original CT ion, we targeted the synthesis of complexes containing $[RuCl([n]aneS_4)]^+$ centers bridged by ligands, such as pyrazine, that contain two monodentate sites. Herein we report on the synthesis and structures of these systems, assess their electrochemical, optical, and electronic properties, and, through computational studies, explore the molecular orbitals involved.

Results and Discussion

Synthetic Studies. We chose to study systems with pyrazine (pyz), 4,4′-bipyridine, (4,4′-bpy), and 3,6-bis(4-pyridyl)-1,2,4,5-tetrazine, (4-bptz) bridges, which provide monodentate coordination to two metal centers at fixed distances of approximately 7, 11, and 13 Å, respectively. Each of these ligands was reacted with the starting material $[Ru([n]aneS_4)(DMSO)Cl]^+$ (again, n = 12, 14, and 16). After heating to reflux for 18 h, addition of NH_4PF_6 followed by filtration of the warm solution resulted in the collection of the complexes as analytically pure solids. Using this method the complexes $[\mathbf{1}](PF_6)_2$−$[\mathbf{9}](PF_6)_2$, Scheme 1, were synthesized.

Structural Studies. X-ray diffraction quality crystals of complexes $[\mathbf{1}](PF_6)_2$, $[\mathbf{3}](PF_6)_2$, and $[\mathbf{6}](PF_6)_2$ were obtained by vapor diffusion of diethyl ether into saturated nitromethane solutions. Selected bond distances and angles in the ruthenium coordination spheres of these three binuclear complexes are summarized in Table 1.

In the structure of $[\mathbf{1}](PF_6)_2$ the pyrazine bridge was found to be disordered over two positions across a center of inversion, which were refined with 50% of occupancy each (see Figure 1). The coordinated chlorides were also found to be disordered over two sites. The equivalent ruthenium(II) ions, which are held 7.037 Å apart, are in a distorted octahedral geometry. One of the *trans*-angles is fairly close to the ideal with a value of 178.7(2)° [N−Ru−S(2)]; however, two are more distorted: [S(1)−Ru−Cl] = 168.1(4)° and [S(4)−Ru−S(4*)] = 166.75(15)°; while the *cis*-angles around the Ru^{II} center range from 78.9(4) to 99.8(3)°. There are slight differences between the Ru−S bonds with the Ru−S(1) being the shortest because of the *trans* influence of the opposite chloride.

The two identical Ru^{II} centers in the structure of $[\mathbf{3}](PF_6)_2$, Figure 2 and Table 1, are less distorted than their analogues in $[\mathbf{1}](PF_6)_2$: for example their *trans*-angles range from 171.93(5)° to 177.21(11)°, and the *cis*-angles around the Ru^{II} center range from 87.64(11)° to 94.71(5)°. This effect has been observed before: the relatively small binding cavity of coordinated $[12]aneS_4$ produces geometries that are distorted away from octahedral symmetry.[13,14] The distance between the two metal centers (7.053 Å) is very close to that of $[\mathbf{1}](PF_6)_2$. Interestingly, whereas the two Ru−Cl bonds in $[\mathbf{1}](PF_6)_2$ are eclipsed, they are staggered in $[\mathbf{3}](PF_6)_2$. This may be a consequence of crystallographic packing interactions or electronic factors (vide infra).

In the structure of $[\mathbf{6}](PF_6)_2$ the Ru^{II} centers are held 11.434 Å apart by a 4,4′-bpy bridge in which the two aromatic rings are coplanar (Figure 3). As for $[\mathbf{3}](PF_6)_2$, the two Ru−Cl bonds are staggered at 180°. The coordination geometry in the two complexes, which both contain $[Ru^{II}[16]aneS_4]$ moieties, is also comparable. For example, *trans*-angles for $[\mathbf{6}](PF_6)_2$ show a very similar distribution (172.88(10)° to

(6) (a) *Electron Transfer in Inorganic, Organic and Biological Systems, Advances in Chemistry Series*; Bolton, J. R., Mataga, N., McLendon, G., Eds.; American Chemical Society: Washington, DC, 1991; p 228. (b) *Electron Transfer in Chemistry*; Balzani, V., de Silva, A. P., Eds.; Wiley-VCH: New York, 2001; Vol. *3*.

(7) (a) Creutz, C. *Prog. Inorg. Chem.* **1983**, *30*, 1. (b) Crutchley, R. J. *Adv. Inorg. Chem.* **1994**, *41*, 372. (c) Kaim, W.; Klein, A.; Glöckle, M. *Acc. Chem. Res.* **2000**, *33*, 755. (d) Launay, J.-P. *Chem. Soc. Rev* **2001**, *30*, 386. (e) Ward, M. D.; McCleverty, J. A. *J. Chem. Soc., Dalton Trans.* **2002**, 275. (f) Kaim, W.; Sarkar, B. *Coord. Chem. Rev.* **2007**, *251*, 584.

(8) (a) Roche, S.; Yellowlees, L. J.; Thomas, J. A. *Chem. Commun.* **1998**, 1429. (b) Araújo, C. S.; Drew, M. G. B.; Félix, V.; Jack, L.; Madureira, J.; Newell, M.; Roche, S.; Santos, T. M.; Thomas, J. A.; Yellowlees, L. J. *Inorg. Chem.* **2002**, *41*, 2260.

(9) Shan, N.; Vickers, S.; Adams, H.; Ward, M. D.; Thomas, J. A. *Angew. Chem., Int. Ed.* **2004**, *43*, 3938.

(10) Shan, N.; Ingram, J. D.; Easun, T. L.; Vickers, S.; Adams, H.; Ward, M. D.; Thomas, J. A. *Dalton Trans.* **2006**, 2900.

(11) Newell, M.; Thomas, J. A. *Dalton Trans.* **2006**, 705.

(12) Newell, M.; Ingram, J. D.; Easun, T. L.; Vickers, S.; Adams, H.; Ward, M. D.; Thomas, J. A. *Inorg. Chem.* **2006**, *45*, 821.

(13) (a) Goodfellow, B. J.; Pacheco, S. M. D.; Pedrosa de Jesus, J. P.; Felix, V.; Drew, M. G. B. *Polyhedron* **1997**, *16*, 3293. (b) Santos, T. M.; Goodfellow, B. J.; Madureira, J.; Pedrosa de Jesus, J.; Félix, V.; Drew, M. G. B. *New J. Chem.* **1999**, *23*, 1015. (c) Pillinger, M.; Gonçalves, I. S.; Lopes, A. D.; Madureira, J.; Ferreira, P.; Valente, A. A.; Santos, T. M.; Rocha, J.; Menezes, J. F. S.; Carlos, L. D. *J. Chem. Soc., Dalton Trans.* **2001**, 1628.

(14) Adams, H.; Amado, A. M.; Félix, V.; Mann, B. E.; Antelo-Martinez, J.; Newell, M.; Ribeiro-Claro, P. J. A.; Spey, S. E.; Thomas, J. A. *Chem.—Eur. J.* **2005**, *11*, 2031.

Scheme 1

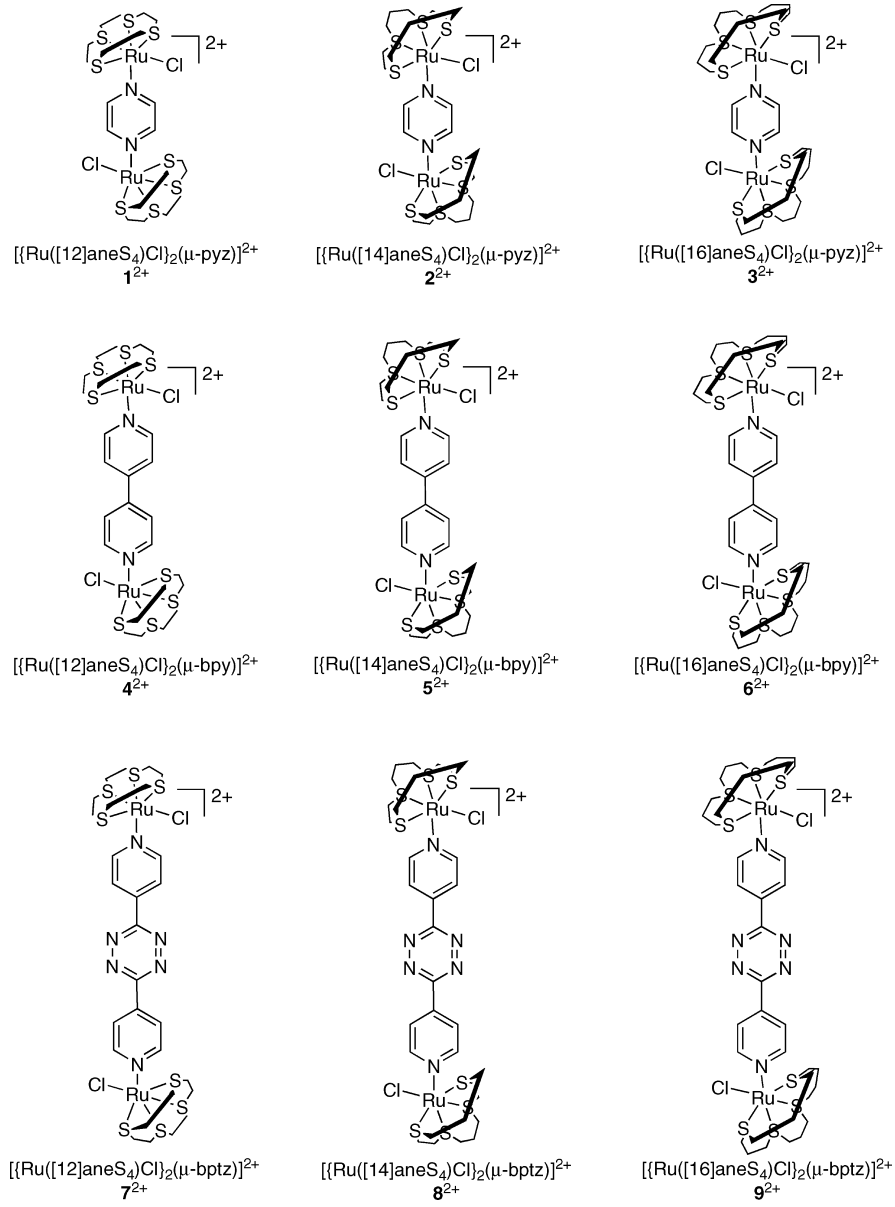

Table 1. Selected Bond Lengths and Bond Angles for Complexes [**1**]$(PF_6)_2$, [**3**]$(PF_6)_2$, and [**6**]$(PF_6)_2$

complex	[1]$(PF_6)_2$	[3]$(PF_6)_2$	[6]$(PF_6)_2$
		Bond Lengths (Å)	
Ru−S(1)	2.253(3)	2.2976(15)	2.300(2)
Ru−S(2)	2.297(5)	2.3190(14)	2.317(2)
Ru−S(3)		2.3597(14)	2.349(3)
Ru−S(4)	2.349(2)	2.3487(14)	2.355(3)
Ru−N	2.116(11)	2.111(4)	2.152(7)
Ru−Cl	2.488(10)	2.4479(14)	2.440(3)
		Bond Angles (deg)	
S(4)−Ru-S(3)	166.75(15)[a]	172.47(5)	172.88(10)
S(2)−Ru-N	178.7(2)	177.21(11)	177.2(2)
S(1)−Ru-Cl	168.1(4)	171.93(5)	173.82(9)
cis-angles			
N−Ru−Cl	78.9(4)	84.09(11)	88.2(2)
S−Ru−S	84.01(8)−92.08(13)	89.33(5)−94.71(5)	89.77(11)−95.29(11)
S−Ru−N	89.2(2)−96.05(8)	88.05(11)−89.2(2)	86.4(2)−88.4(2)
S−Ru−Cl	93.80(6)−99.8(3)	87.64(11)−94.66(5)	85.02(10)−92.95(10)

[a] In [1]$(PF_6)_2$ this angle corresponds to S(4)−Ru-S(4*) where * is the symmetry operation $0.5 - x$, $0.5 - y$, $0.5 - z$ (see Figure 1).

177.2(2)°) to that found in [**3**]$(PF_6)_2$. However, the Ru−N bond length in $\mathbf{6}^{2+}$ (2.152(7) Å) appears to be noticeably longer than that in $\mathbf{1}^{2+}$ or $\mathbf{3}^{2+}$ (2.116(11) Å and 2.111(4) Å, respectively), although this may be an artifact because of

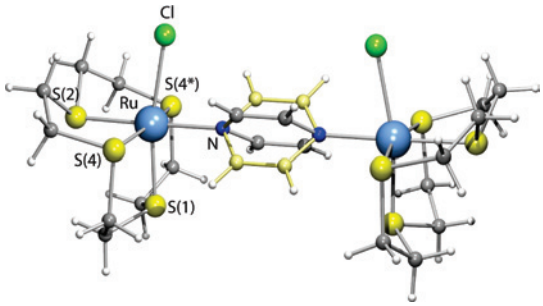

Figure 1. PLUTON plot of the cation in [**1**][$(PF_6)_2$], showing the two alternative positions of the disordered bridging ligand. The chlorides are presented only in one of the disordered positions (* denotes the symmetry operation: 0.5 − *x*, 0.5 − *y*, 0.5 − *z*).

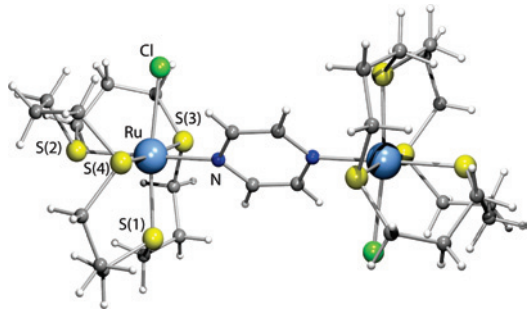

Figure 2. PLUTON plot of the cation in [**3**][$(PF_6)_2$].

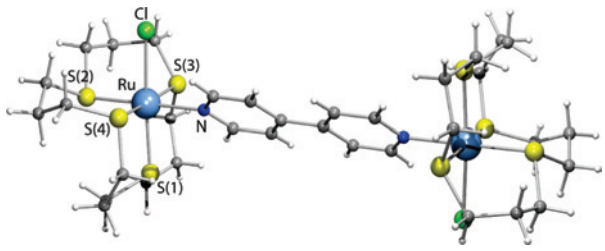

Figure 3. PLUTON plot of the cation in [**6**][$(PF_6)_2$].

the poorer quality of the structural data for **6**. A more noticeable difference between the three structures is the dihedral angle between the plane of the bridging ligand and the equatorial plane of the metal coordination spheres defined by three S-donors and the N-donor of the bridge (ω). In all three structures these planes are not parallel; in [**1**]$(PF_6)_2$ the two planes are held at 32.79°, given by the two alternative pyrazine disordered orientations, while the corresponding angle in the other pyrazine bridged structure, [**3**]$(PF_6)_2$ is 46.67°. For [**6**]$(PF_6)_2$ this angle is 39.61°.

Electrochemistry Studies. Coupling between metal centers in MV states of the new complexes was first probed through cyclic voltammetry (CV). The results of these studies are summarized in Table 2. In addition to a variety of ligand-based reduction processes, all the complexes displayed reversible oxidation couples, the nature of which was highly dependent on the bridging ligand involved. Complexes **1**−**3** all displayed processes that can be assigned to $Ru^{III/II}$ couples.

As the CV of [**1**]$(PF_6)_2$, shown in Figure 4, illustrates, a close inspection of the oxidations reveals that each process is not a one-electron couple. Similar electrochemical behavior has been observed for previously reported [{Ru([n]-ane-S_4)}$_2$(μ-dpp)]$^{4+}$ systems[11] and, just as in that case, interpretation of the data for **1**−**3** was greatly facilitated by an analysis of their $dI1/dE$ versus E deconvolutions.[15]

Table 2. Summary of Electrochemical Data for the Hexafluorophosphate Salts of Complexes **1**−**9** vs Ag/AgCl in Acetonitrile

complex	$E_{1/2}(1)$/V	$E_{1/2}(2)$/V	ΔE (mV)	K_c[a]
$\mathbf{1}^{2+}$	1.36	1.45	90	35
$\mathbf{2}^{2+}$	1.32	1.43	110	75
$\mathbf{3}^{2+}$	1.37	1.46	90	35
$\mathbf{4}^{2+}$	1.20[b]			
$\mathbf{5}^{2+}$	1.15[b]			
$\mathbf{6}^{2+}$	1.21[b]			
$\mathbf{7}^{2+}$	1.30[b]			
$\mathbf{8}^{2+}$	1.20[b]			
$\mathbf{9}^{2+}$	1.32[b]			

[a] Calculated using the relationship log $K_c = \Delta E/0.059$. [b] Two unresolved coincident redox processes.

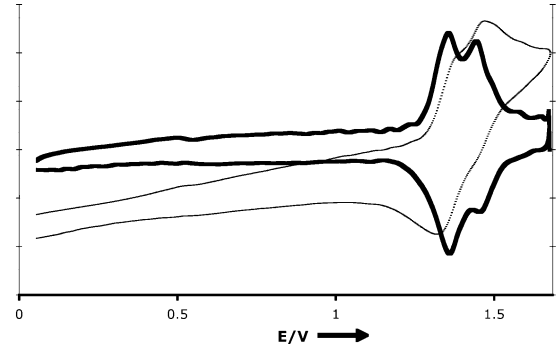

Figure 4. Metal based oxidation couples for **1.** Cyclic voltammogram (fine line) and $dI1/dE$ vs E deconvolutions (bold line).

This transform is equivalent to a differential pulse polarogram with infinitely small pulse amplitude and an additional reverse sweep. For electrochemically reversible processes, peaks of the forward and reverse sweeps align at the potential of $E_{1/2}$, while chemical reversibility is indicated by forward and return peaks of equal but opposite amplitude.[16] The $dI1/dE$ versus E deconvolutions of the cv data for complexes **1**−**3** reveal that the first couple for all the complexes displays good reversibility, while the second oxidation is not completely chemically reversible (see Figure 4).

Using the relationship log $K_c = \Delta E/0.059$ and the values of ΔE obtained from an analysis of the electrochemistry data, we also obtained estimates for the comproportionation constants for these complexes (see Table 2). These K_c values are considerably smaller than the CT-ion ($K_c = 10^{6.6}$)[1] but are of the same order as K_c values for other pyrazine systems containing π-acceptor ligands, such as [$(bpy)_2$ClRu(μ-pyz)RuCl$(bpy)_2$]$^{5+}$ ($K_c = 160$).[17]

In contrast, the voltammograms (and deconvolutions) of complexes **4**−**9** all display a single two coincident one electron couples suggesting that is little or no interaction between metal centers in these complexes.

UV/vis Spectroscopic Studies. The UV/vis spectra of compounds **1**−**9** were recorded in acetonitrile solvent. Each of the nine complexes shows two distinct bands (see Table

(15) Bard, A. J.; Faulkner, L. R. *Electrochemical Methods. Fundamentals and Applications*, 2nd ed.; Wiley: New York, 2001.
(16) Imbeau, J.-C.; Saveant, J.-M. *J. Electroanal. Chem.* **1973**, *44*, 169.
(17) Goldsby, K. A.; Meyer, T. J. *Inorg. Chem.* **1984**, *23*, 3002.

Table 3. UV/vis Data for Complexes **1**−**9**

complex[a]	λ_{max} (nm)	ε (dm^3 mol^{-1} cm^{-1})	assignment
$\mathbf{1}^{2+}$	204	51400	π-π*
	468	7900	MLCT
$\mathbf{2}^{2+}$	210	50300	π-π*
	460	5000	MLCT
$\mathbf{3}^{2+}$	213	49000	π-π*
	456	3300	MLCT
$\mathbf{4}^{2+}$	243	28200	π-π*
	391	13500	MLCT
$\mathbf{5}^{2+}$	245	27400	π-π*
	383	12500	MLCT
$\mathbf{6}^{2+}$	246	32000	$\pi\pi$*
	394	10800	MLCT
$\mathbf{7}^{2+}$	264	21100	π-π*
	389	10800	MLCT
$\mathbf{8}^{2+}$	272	18100	π-π*
	379	12600	MLCT
$\mathbf{9}^{2+}$	270	16700	$\pi\pi$*
	385	10700	MLCT

[a] For hexafluorophosphate salts in acetonitrile.

3). The first band, between 200−300 nm, has a large absorption coefficient and by comparison to related complexes it has been assigned to a π-π* transition. The second of the bands is observed between 370−470 nm and is assigned as a metal-to-ligand charge-transfer (MLCT) transition involving the bridging ligand.

Spectroelectrochemical Studies. Since electrochemically derived comproportionation constants do not always provide an accurate picture of electronic coupling in MV systems,[8,18−20] UV−visible absorption spectroelectrochemistry was used to further investigate the interaction between the metal centers of complexes **1** to **3**. These studies were carried out on hexafluorophosphate salts under a dinitrogen atmosphere in acetonitrile using an optically transparent thin-layer electrochemical (OTTLE) cell thermostatted at 253 K. All three complexes show very similar behavior. The two individual $Ru^{III/II}$ couples for **1**, **2**, and **3** are sufficiently separated to allow clean electrochemical generation of the MV state: as expected from the electrochemical studies, the first one-electron oxidation of each of the complexes is entirely reversible with several isosbestic points being observed, furthermore, after reduction back to the starting oxidation state, absorption spectra overlay those obtained at the start of the experiment. In all cases, significant changes are observed in the Ru(d)→pyz(π*) MLCT band. For example, during the $\mathbf{1}^{2+}\rightarrow\mathbf{1}^{3+}$ oxidation the band centered at 468 nm diminishes and growth of a relatively weak, low energy band at 1244 nm (8040 cm^{-1}) is observed (see Figure 5). The structure of this new band is more easily seen in the [$\mathbf{1}^{3+}-\mathbf{1}^{2+}$] difference spectrum (inset in Figure 5). The position, size and shape of this band are consistent with intervalence charge transfer, IVCT, bands observed in similar $Ru^{III/II}$ MV systems. While similar bands are also seen when $\mathbf{2}^{3+}$ and $\mathbf{3}^{3+}$ are generated, a comparison of these features show that they differ slightly (see Table 4).

It is notable that the near-infrared, NIR, band for $\mathbf{1}^{3+}$ is asymmetric with narrower half-bandwidths on the high-energy side of the IVCT. IVCT band asymmetries are observed for systems at the Class II/III interface whereas solvent interactions are averaged, but these asymmetries are observed as narrow half-bandwidths on the *low energy side* of the transition. However, asymmetric structuring can also be observed in MV systems whereas a combination of the low ligand set symmetry, extensive orbital mixing and spin orbit coupling leads to d$\pi^{5/6}$ states being split into Kramer doublets, thus allowing multiple IVCTs.[4a,9,10,21,22] In contrast to $\mathbf{1}^{3+}$, the equivalent bands for $\mathbf{2}^{3+}$ and $\mathbf{3}^{3+}$ are symmetrical. According to Hush theory[23] for Class II systems: $\Delta\nu_{1/2} = (2310\nu)^{1/2}$ cm^{-1} where $\Delta\nu_{1/2}$ = width of the band at half height. A comparison of the data for complexes **1**−**3** shows some disparities between experimental and calculated figures (see Table 3).

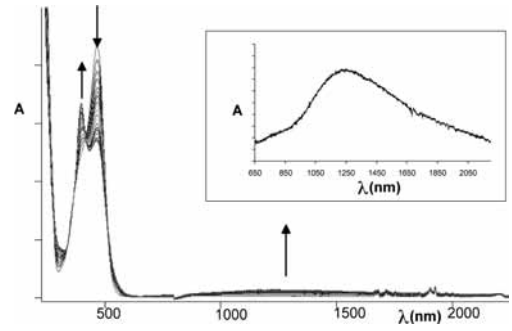

Figure 5. Spectroelectrochemistry spectra showing the oxidation of $\mathbf{1}^{2+}$ to $\mathbf{1}^{3+}$. Inset: details of the [$\mathbf{1}^{3+}-\mathbf{1}^{2+}$] difference spectrum.

Table 4. Details of Intervalence Charge Transfer Bands Observed for Complexes 1^{3+}−3^{3+} in Acetonitrile

complex	λ_{max} (nm) (ν_{max}(cm^{-1}))	ε (M^{-1} cm^{-1})	$\Delta\nu_{1/2}$[expt] (cm^{-1})	$\Delta\nu_{1/2}$[calc] (cm^{-1})[a]
$\mathbf{1}^{3+}$	1244(8040)	170	3950	4310
$\mathbf{2}^{3+}$	1315(7605)	375	5200	4190
$\mathbf{3}^{3+}$	1447(6910)	175	4505	3995

[a] Calculated using $\Delta\nu_{1/2} = (2310\nu)^{1/2}$ cm^{-1}.

Of the three complexes, $\mathbf{1}^{3+}$ shows the shortest wavelength IVCT. Significantly, the value of $\Delta\nu_{1/2}$(calc) is larger than the experimentally derived figure. In fact, for systems like $\mathbf{1}^{3+}$ the value of $\Delta\nu_{1/2}$(expt) is probably slightly overestimated because, as discussed above, the observed NIR band is composed of several overlapping IVCTs. Since the IVCT for $\mathbf{1}^{3+}$ is still narrower than predicted, we conclude that it is clearly a Class III (valence delocalized) system. Consequently,[4,7,23] the extent of electronic coupling (H_{AB}) in this system can be assessed as approximately [$\Delta\nu_{max}/2$] = 4020 cm^{-1}.

In contrast, while both $\mathbf{2}^{3+}$ and $\mathbf{3}^{3+}$ do have IVCT bands, these are appreciably wider than theoretical predictions, with this discrepancy being larger for $\mathbf{2}^{3+}$. Even allowing for the effect of multiple transitions, it seems likely that these systems are Class II. Therefore, the value of H_{AB} was estimated using

(18) Ferrere, S.; Elliott, C. M. *Inorg. Chem.* **1995**, *34*, 5818.
(19) Yeomans, B. D.; Humphrey, D. G.; Heath, G. A. *Dalton Trans* **1997**, 4153.
(20) D'Alesandro, D. M.; Keene, F. R. *Dalton Trans.* **2004**, 3950.
(21) Kober, E.; Goldsby, K. A.; Narayana, D. N. S.; Meyer, T. J. *J. Am. Chem. Soc.* **1983**, *105*, 4303.
(22) (a) Kasack, V.; Kaim, W.; Binder, J. H.; Jordanov, J.; Rothl, E. *Inorg. Chem.* **1995**, *34*, 1924. (b) Moscherosch, M.; Waldhör, E.; Binder, H.; Kaim, W.; Fiedler, J. *Inorg. Chem.* **1995**, *34*, 4326.
(23) (a) Hush, N. S. *Prog. Inorg. Chem.* **1967**, *8*, 391. (b) Hush, N. S. *Electrochim. Acta* **1968**, *13*, 1005. (c) Hush, N. S. *Coord. Chem. Rev.* **1985**, *64*, 135.

$$H_{AB} = \frac{2.06 \times 10^{-2}}{R}(\nu_{max}\varepsilon_{max}\Delta\nu_{1/2})^{1/2}$$

where R is the transition dipole length usually approximated by intermetallic distances obtained from structural studies on the isovalent form.[4,7,23] Despite the distortions created by the anomalous coordination demands of [12]aneS$_3$ (vide ultra), in both $\mathbf{1}^{2+}$ and $\mathbf{3}^{2+}$ this distance is almost identical, being 7.037 Å and 7.053 Å, respectively. Crystallographic studies on related systems have demonstrated that there is an even stronger structural similarity between structures incorporating [Ru^{II}[14]aneS$_3$] and [Ru^{II}[16]aneS$_3$] units. Therefore, since a crystal structure for [**2**](PF$_6$)$_2$ was not obtained, the Ru−Ru distance found in $\mathbf{3}^{2+}$ was also used in the calculation of H_{AB} for $\mathbf{2}^{3+}$, yielding values of 355 cm^{-1} and 215 cm $^{-1}$ for $\mathbf{2}^{3+}$ and $\mathbf{3}^{3+}$, respectively.

As the electrochemical studies discussed in the previous section indicated, the second oxidation for all three complexes were clearly not chemically reversible: absorption spectra after the return reduction were not superimposable on the original spectra, and thus the optical properties of the intact isovalent [Ru^{III}/Ru^{III}] state could not be assigned with any confidence. Furthermore, since complexes **4**−**9** all display two coincident couples it was not possible to investigate any evidence of electronic interactions in these systems' MV states.

Computational Studies. To gain further insight into the changes in the extent of interaction between the metal centers of complexes **1**−**9**, density-functional theory (DFT) studies were carried out on $\mathbf{1}^{2+}$, $\mathbf{3}^{2+}$, and $\mathbf{6}^{2+}$. Using the experimental X-ray data as a starting point, these structures were fully optimized at the DFT (B3LYP) level of theory. Supporting Information, Table S1 presents a summary of selected calculated interatomic distances and angles compared with X-ray diffraction data. The labeling scheme was the same adopted for the X-ray structural studies.

For the three complexes, the two ruthenium centers are calculated in a distorted octahedral geometry. The experimental Ru···Ru interatomic distances, as well as the Ru−N and Ru−Cl bond lengths, are satisfactorily reproduced in our calculations, but the calculated Ru−S bond lengths are systematically longer than the experimental ones by 0.07 Å (mean deviation for the three complexes). However, the experimental trends are correctly reproduced, for example; the Ru−S(3) and Ru−S(4) distances are systematically longer than the remaining Ru−S distances. The corresponding angle S(3)−Ru−S(4) (167°) in the 12-membered macrocycle complex $\mathbf{1}^{2+}$ is more different from ideal *trans* octahedral angle (180°), as found in the X-ray structure, reflecting the small cavity size of the [12]aneS$_4$. By contrast, in the largest 16-membered macrocycle complexes ($\mathbf{3}^{2+}$ and $\mathbf{6}^{2+}$), the calculated angles are only ∼7° away from the ideal value, which are also very similar to the experimental ones. The calculated dihedral angles between the plane of the bridging ligand and the equatorial coordination planes (ω, vide supra) for $\mathbf{1}^{2+}$ are 46°, which is 13° different from the observed value. However, it should be emphasized that in the X-ray structure the pyrazine bridging ligand is disordered over two positions, and consequently, this angle is not accurately determined. Indeed, for $\mathbf{3}^{2+}$ the calculated angles (48°) are in excellent agreement with the experimental ones (47°). The X-ray structure of $\mathbf{6}^{2+}$ shows an almost planar 4,4′-bpy bridge, with the angle between the two aromatic rings (τ) equal to 2° whereas in the optimized structure, this unit is twisted by 33° which is in agreement with experimental observations for free 4-4′-bipy (τ = 41°),[24] and the related biphenyl structure (τ = 44°).[25] Indeed, the planar (τ = 0°) or orthogonal (τ = 90°) arrangements of free 4-4′-bipy correspond to transition states on the potential energy surface.[26] When coordinated and in the solid state, packing forces should be strong enough to overcome the steric repulsions of the *ortho* hydrogens, forcing the 4,4′-bpy bridge to remain planar. The packing effects are not taken into account in our calculations and therefore the lowest energy twisted structure is obtained. In line with this observation it is not surprising that the calculated dihedral angles ω (53° and 55°) are not comparable with the crystallographically determined ones (∼40°).

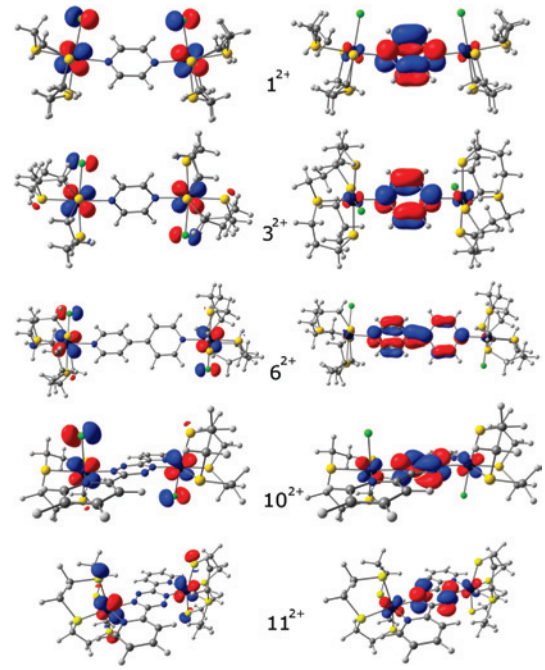

Figure 6. HOMOs (left) and LUMOs (right) of complexes $\mathbf{1}^{2+}$, $\mathbf{3}^{2+}$, $\mathbf{6}^{2+}$, $\mathbf{10}^{2+}$, and $\mathbf{11}^{4+}$.

The highest occupied molecular orbitals (HOMOs) and lowest unoccupied molecular orbitals (LUMOs) of complexes $\mathbf{1}^{2+}$, $\mathbf{3}^{2+}$, and $\mathbf{6}^{2+}$ are depicted in Figure 6. For comparison purposes, the geometries of the related and previously reported[12] complexes [RuCl([9]aneS$_3$)(bpta)]$_2^{2+}$ ($\mathbf{10}^{2+}$) and [Ru([12]aneS$_4$)(bpta)]$_2^{4+}$ ($\mathbf{11}^{4+}$) (bpta = 3,6-bis(2-pyridyl)-1,2,4,5-tetrazine, see Scheme 2) with bis-bidentate bridging

(24) Nather, C.; Riedel, J.; Jess, I. *Acta Crystallogr., Sect.C: Cryst. Struct. Commun.* **2001**, *57*, 111.
(25) Almenningen, A.; Bastiansen, O.; Fernholt, L.; Cyvin, B. N.; Cyvin, S. J.; Samdal, S. *J. Mol. Struct.* **1985**, *128*, 59.
(26) Perez-Jimenez, A. J.; Sancho-Garcia, J. C.; Perez-Jorda, J. M. *J. Chem. Phys.* **2005**, *123*, 134309.

Scheme 2

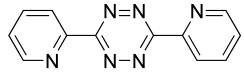

bpta

ligands were also optimized and their HOMO and LUMO are also represented in Figure 6.

The detailed composition of the frontier MOs can be found in Supporting Information, Tables S2, S3, and S4.

The calculations indicate that the main character of these MOs is largely independent of the macrocycle, the bridging ligand, or the chloride ligand. The HOMOs are out-of-phase metal centered orbitals, with some contribution from the chlorine (for $\mathbf{1}^{2+}$, $\mathbf{3}^{2+}$, $\mathbf{6}^{2+}$, and $\mathbf{10}^{2+}$, which can be described as Ru−Cl π* orbitals). The LUMOs are π* orbitals localized on the bridging ligand. However, some subtle differences can be found in the MO compositions: the replacement of the macrocycle from $\mathbf{1}^{2+}$ to $\mathbf{3}^{2+}$ (i.e., [12]aneS$_4$ by [16]aneS$_4$) causes a decrease on the participation of the metals in the LUMOs from ∼17% to ∼13%.

The same effect is observed by changing the bridging ligand pyz to 4,4′-bpy ($\mathbf{3}^{2+}$ to $\mathbf{6}^{2+}$; ∼13% to 9%). In replacing monodentate bridging ligands ($\mathbf{1}^{2+}$, $\mathbf{3}^{2+}$, $\mathbf{6}^{2+}$) with bidentate bridges ($\mathbf{10}^{2+}$, $\mathbf{11}^{4+}$), the most striking difference observed is the higher metal participation in the LUMO (>20%). Complexes $\mathbf{1}^{2+}$ and $\mathbf{3}^{2+}$ show a first reversible oxidation at 1.36 and 1.37 V, respectively, which are centered on the ruthenium, as shown by the HOMO character.

The structures of the oxidized complexes $\mathbf{1}^{2+}$, $\mathbf{3}^{2+}$, and $\mathbf{6}^{2+}$ were also studied by means of DFT optimizations. Selected interatomic distances and angles for the oxidized species are also reported in Supporting Information, Table S1. No significant structural changes are observed upon oxidation, and all oxidized complexes retain their distorted octahedral geometry. The removal of electrons from the Ru−Cl π* HOMO causes a slight shortening of the Ru−Cl bonds, and consequently, the Ru−S(1) distances are elongated. No substantial changes are observed for the remaining distances within 0.05 Å, as well as for the N−Ru−Cl, S(3)−Ru−S(4), or Cl−Ru−Ru−Cl angles.

Subsequently, using the optimized structures, we performed time-dependent density-functional theory (TD-DFT) calculations on the selected complexes, and the oxidized forms $\mathbf{1}^{3+}$ and $\mathbf{3}^{3+}$, to further investigate the experimental UV/vis and spectroelectrochemistry assignments. Again, for comparison purposes, the TD-DFT spectrum was also calculated for $\mathbf{10}^{2+}$ and $\mathbf{11}^{4+}$. Typically, the lowest-energy fifteen excitations were calculated, but only the relevant excitations are shown in Table 5.

For $\mathbf{1}^{2+}$, several excitations with negligible oscillator strength are calculated in the 513−400 nm range and only two strong absorptions are present, at 505 and 408 nm. While the first excitation corresponds to an almost pure HOMO to LUMO transition, the second is due to a HOMO-4 to LUMO excitation. Both HOMO and HOMO-4 are localized on the ruthenium centers, displaying Ru−Cl π* character, while the LUMO is a pyrazine localized orbital (see Figure 7, left). In the experimental spectrum in acetonitrile solution, only one absorption is observed at λ_{max} = 468 nm. However, as reported earlier for $\mathbf{10}^{2+}$,[12] this band is a merger of the two transitions because of the bathochromic shift of the higher-energy band. Therefore, the experimentally observed band corresponds to a superposition of the calculated transitions at 505 and 408 nm. Nevertheless, the experimental band is incontrovertibly assigned as a charge transfer from ruthenium d orbitals to a π* orbital located on the pyrazine ring (MLCT). Taking into account that modeling is on a charged species in vacuum, the agreement between experimental and calculated values is good; indeed, comparable discrepancies have arisen in calculations on other charged transition-metal complexes.[27]

Table 5. Most Relevant TD-DFT Excitation Energies (λ), Compositions, and Oscillator Strengths (OS) for Complexes $\mathbf{1}^{2+}$, $\mathbf{3}^{2+}$, $\mathbf{6}^{2+}$, $\mathbf{10}^{2+}$, and $\mathbf{11}^{2+}$ and their Oxidized Forms ($\mathbf{1}^{3+}$, $\mathbf{3}^{3+}$) Compared with Experimental Data (λ_{exp})

complex	composition	λ (nm)	OS	λ_{exp} (nm)	assignment
$\mathbf{1}^{2+}$	H → L (85%)	505	0.1884	468	MLCT ($d_{Ru} \rightarrow \pi^*$)
	H-4→ L (79%)	408	0.2130		
$\mathbf{1}^{3+}$	$H_\beta \rightarrow L_\beta$ (37%)	3021	0.1056	1244	MMCT/IVCT
	$H2_\beta \rightarrow L_\beta$(10%)				
$\mathbf{3}^{2+}$	H → L (83%)	500	0.1237	456	MLCT ($d_{Ru} \rightarrow \pi^*$)
	H-4 → L (87%)	426	0.1624		
$\mathbf{3}^{3+}$	H-$2_\beta \rightarrow L_\beta$ (49%)	3136	0.0584	1447	MMCT/IVCT
	$H_\beta \rightarrow L_\beta$ (20%)				
	H-$4_\beta \rightarrow L_\beta$ (10%)				
$\mathbf{6}^{2+}$	H → L (92%)	483	0.0948	394	MLCT ($d_{Ru} \rightarrow \pi^*$)
	H-4 → L (84%)	406	0.2603		MLCT ($d_{Ru} \rightarrow \pi^*$)
$\mathbf{10}^{2+}$	H → L (+53%)	687	0.1697	751[a]	MLCT ($d_{Ru} \rightarrow \pi^*$)
	H→ L+1(+22%)				
	H-1→L+1(+75%)	607	0.1074		
	H →L (12%)				
$\mathbf{11}^{4+}$	H → L (67%)	720	0.1504	716[a]	MLCT ($d_{Ru} \rightarrow \pi^*$)
	H-4 → L (18%)				
	H-4 → L (49%)	536	0.3666	528[a]	MLCT ($d_{Ru} \rightarrow \pi^*$)
	H → L+1 (20%)				
	H → L (12%)				

[a] Values taken form from ref 12.

As discussed above, the experimental UV/vis spectrum of $\mathbf{1}^{3+}$, obtained by spectroelectrochemistry, shows a new low-energy band at 1244 nm (8040 cm^{-1}) which is consistent with a valence delocalized system. Indeed, the spin densities at each ruthenium, derived from a Mulliken Population Analysis (MPA), are equal (0.4). However, these conclusions must be analyzed with care when they are dealing with localized versus delocalized predictions based on conventional DFT (vide infra). The calculated TD-DFT spectrum does show a new low energy excitation, but the difference between calculated (3021 nm; 3310 cm^{-1}) and experimental values is quite large. However, large deviations from experimental values in TD-DFT spectra of mixed-valence complexes are not unusual. For example, even for 0/+1 pairs, such as [RhL$_2$-{η^5-(2-ferrocenyl)indenyl}],[28] the difference between calculated and experimental values is still large (∼1250 cm^{-1}). The main contribution for the low-energy transition calculated at 3021 nm is an excitation from the HOMO$_\beta$ to LUMO$_\beta$, which corresponds to HOMO of $\mathbf{1}^{2+}$, mixed with HOMO-2$_\beta$ to LUMO$_\beta$ excitation. Analyzing the

(27) Pereira, C. C. L.; Costa, P. J.; Calhorda, M. J.; Freire, C.; Rodrigues, S. S.; Herdtweck, E.; Romão, C. C. *Organometallics* **2006**, *25*, 5223–5234.

(28) Santi, S.; Orian, L.; Durante, C.; Bisello, A.; Benetollo, F.; Crociani, L.; Ganis, P.; Ceccon, A. *Chem.—Eur. J.* **2007**, *13*, 1955–1968.

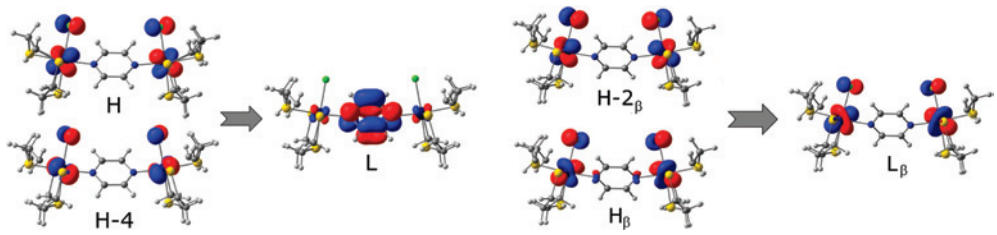

Figure 7. Kohn−Sham molecular orbitals involved in the electronic transitions of complex $\mathbf{1}^{2+}$ (left) and its oxidized product $\mathbf{1}^{3+}$ (right).

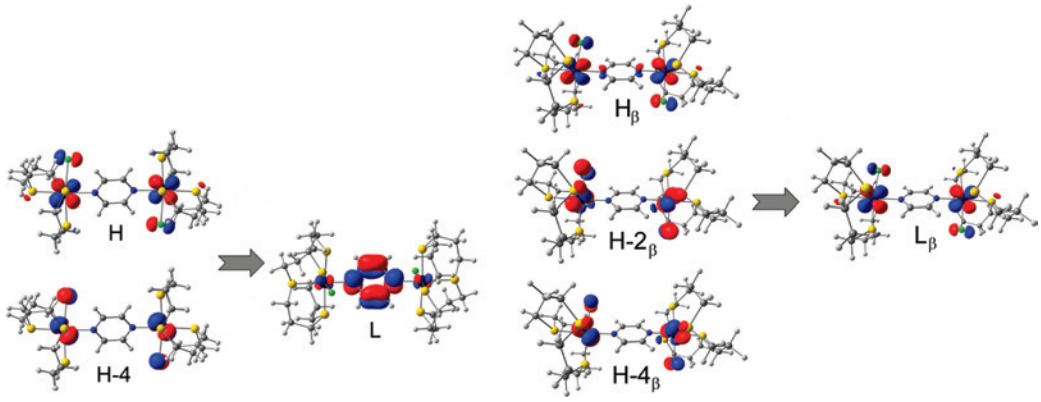

Figure 8. Kohn−Sham molecular orbitals involved in the electronic transitions of complex $\mathbf{3}^{2+}$ (left) and its oxidized product $\mathbf{3}^{3+}$ (right).

orbitals presented in Figure 7 (right), one can see that HOMO$_\beta$, HOMO-2$_\beta$, and LUMO$_\beta$ have extremely similar character, being ruthenium-centered orbitals, indicating that the calculated transition clearly *does* involve both metal centers.

The TD-DFT calculations performed on the $\mathbf{3}^{2+}/\mathbf{3}^{3+}$ pair produced similar results to those found for $\mathbf{1}^{2+}/\mathbf{1}^{3+}$, despite the fact that the experimental data for $\mathbf{3}^{3+}$ suggests a Class II system. Again, HOMO to LUMO (500 nm) and HOMO-4 to LUMO (426 nm) excitations are calculated with strong oscillator strengths for $\mathbf{3}^{2+}$. Both are assigned as MLCT from ruthenium-based d orbitals to a π^* orbital located on the pyrazine ring, Figure 8 (left), and correspond to the experimentally observed absorption band centered at 456 nm.

For $\mathbf{3}^{3+}$, the spin densities at *each* ruthenium are calculated as 0.45. All attempts to obtain a localized solution failed. DFT over-delocalizes the unpaired electron because of self-repulsion, and the predictions are questionable when dealing with localized versus delocalized systems.[29] In fact, even for a well established Class II symmetric mixed-valence compound such as tetrathiafulvalene-diquinone,[30] DFT fails to obtain an asymmetric structure corresponding to electron localization.[29] The TD-DFT spectrum shows an excitation at 3136 nm, corresponding to a HOMO-2$_\beta$, HOMO$_\beta$ (SOMO), and HOMO-4$_\beta$ to LUMO$_\beta$ transitions. All these are ruthenium d orbitals, while LUMO$_\beta$ is very similar to the SOMO. These excitations are also metal centered transitions associated with the intravalence charge transfer (IVCT) bands, observed at 1447 nm in acetonitrile solution. Once again the deviation of the calculated value from the experimental one is large. This offers further evidence that, despite the accuracy of the TD-DFT calculations in the prediction and interpretation of the isovalent Ru(II)−Ru(II) species, the results for the mixed-valence complexes should only be interpreted qualitatively.

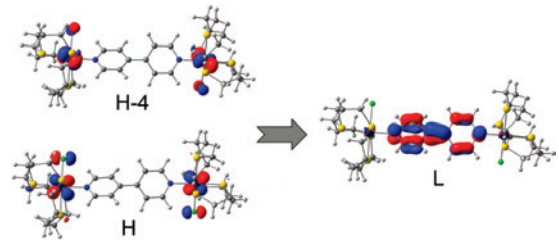

Figure 9. Kohn−Sham molecular orbitals involved in the electronic transitions of complex $\mathbf{6}^{2+}$.

We also calculated the TD-DFT spectra of $\mathbf{6}^{2+}$ whose results are also given in Table 4. Relative to $\mathbf{1}^{2+}$ and $\mathbf{3}^{2+}$, the experimental MLCT absorption band of $\mathbf{6}^{2+}$ moves to higher energies. This trend is reproduced in the theoretical calculations. Two high-energy excitations, again derived from HOMO and HOMO-4 to LUMO transitions (Figure 9), are calculated to appear at 483 and 406 nm. Despite the shift to higher energy, the character of the observed band is still attributed to a MLCT.

A similar analysis for the bidentate bridged complexes, $\mathbf{10}^{2+}$ and $\mathbf{11}^{4+}$, again results in two strong low-energy excitations being calculated. For $\mathbf{10}^{2+}$, a HOMO to LUMO (687 nm) and HOMO-1 to LUMO+1 (607 nm) transitions appear to correspond to the reported band at 751 nm. As can be seen in Figure 6, the HOMO to LUMO transition can be assigned as a charge transfer from a ruthenium d orbital to a π^* orbital located on the bridging ligand. However this excitation also contains appreciable metal centered character because of their increased participation in the LUMO. The HOMO-1 to LUMO+1 excitation (667 nm) is a MLCT without MMCT admixture since the participation of ruthenium in L+1 is negligible (see Figure 10).

In contrast to the other complexes, the experimental UV−vis spectrum of $\mathbf{11}^{4+}$ displays two low energy bands

(29) Wu, Q.; Van Voorhis, T. *J. Phys. Chem. A* **2006**, *110*, 9212–9218.
(30) Gautier, N.; Dumur, F.; Lloveras, V.; Vidal-Gancedo, J.; Veciana, J.; Rovira, C.; Hudhomme, P. *Angew. Chem., Int. Ed.* **2003**, *42*, 2765.

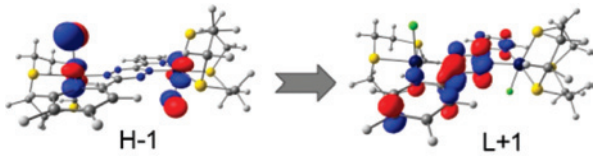

Figure 10. Kohn−Sham molecular orbitals involved in the calculated (667 nm) electronic transition of complex $\mathbf{10}^{2+}$.

at 716 and 528 nm. These are calculated at 720 and 536 nm, respectively, an excellent agreement even without consideration of solvent effects. The calculated lowest-energy band is mainly a HOMO to LUMO transition. Since the HOMO is a metal centered orbital (with sulfur contribution, since there are no chlorine ligands) and the LUMO is a π^* orbital located on the bridging ligand, this transition is MLCT, having, like the previous cases, some MMCT character.

Another point worth mentioning is that for $\mathbf{1}^{2+}$, $\mathbf{3}^{2+}$, $\mathbf{6}^{2+}$, and $\mathbf{10}^{2+}$ the two calculated lowest-energy excitations are relatively close with a gap of <90 nm and only one band is observed experimentally. In contrast, for $\mathbf{11}^{4+}$ the calculated excitations are more separated, being 184 nm apart, and two bands are observed in the experimental spectra. Again this demonstrates that experimentally observed trends are being reproduced in these calculations.

Conclusions

The electronic properties of the nine complexes discussed in this paper vary greatly. The pyrazine bridge systems, **1**−**3**, all display two separate metal-based oxidation couples. While optical and computational studies confirm that these species are electronically interacting, there are some differences in these analyses. DFT calculations confirm that all three systems display metal−metal interactions but there is no qualitative difference between the systems. On the other hand experimental data shows that the IVCT band for $\mathbf{1}^{3+}$ is narrower and at higher energy than those of $\mathbf{2}^{3+}$ and $\mathbf{3}^{3+}$ suggesting that complex $\mathbf{1}^{3+}$ is a Class III system while the other two are Class II. In all probability this discrepancy is due to the DFT based calculations overestimating the electronic delocalization phenomenon. Comparisons with other $Ru^{III/II}$-based pyrazine bridged systems reveal clear trends. The oxidation couples for the new complexes all show a large anodic shift compared to values found for the CT ion, indeed they are anodically shifted compared to systems that incorporate typical π-accepting pyridyl-based ligands. For example the Ru^{II}-based oxidation of $[(bpy)_2ClRu(\mu\text{-}pyz)RuCl(bpy)_2]^{5+}$ occur at +0.93 and +1.05 V (vs Ag/AgCl). These observations are consistent with the electron accepting capabilities of the thiacrown ligands: in coordinated thiacrown ligands donation from metal ion d-orbitals into C−S-bond σ^* orbitals occurs.[8−12,31] This interaction reduces the electron density available for delocalization across the bridging pyrazine; such effect usually lead to an increase in the electron-transfer barrier and consequent decrease in electron transfer rates.[4] Indeed, the intensity and shape of the IVCTs for $\mathbf{1}^{3+}$, $\mathbf{2}^{3+}$, and $\mathbf{3}^{3+}$ in comparison to that of the CT ion are indicative of weaker interactions. This hypothesis is confirmed by the observation that no *electrochemical* interaction between metal centers is observed for complexes **4**− **6**; in contrast, the complex $[\{Ru(NH_3)_5\}_2(4,4'\text{-bpy})]^{5+}$ displays a significant distortion of its CV compared to a single electron redox process[32] and an IVCT analysis reveals that it is a typical example of a Class II system.

It should be noted that although there is no visible *electrochemical* interaction between the metal centers of complexes **4**−**9** this does not indicate an absence of *electronic* coupling within these systems: IVCT bands are observed for the dipyridyl alkene bridged analogues of $[\{Ru(NH_3)_5\}_2(4,4'\text{-bpy})]^{5+}$ even though these systems display two coincident $Ru^{III/II}$ redox couples.[33]

Turning back to the pyrazine bridged complexes, it is notable that although **1**−**3** all possess thiacrown ligands with the same S_4 donor set, their IVCT bands differ slightly in energy and shape. We have observed similar effects on related systems involving bridging ligands with two bidentate sites; but in these cases the differences, particularly in electrochemical properties, were larger. In these cases the effects were rationalized by a consideration of the coordination preferences of the three different [*n*]-ane-S_4 ligands and the extent of C−S σ^*/t_{2g} orbital overlap; however, in this case structural and computational studies provide somewhat conflicting evidence. As previous DFT studies have confirmed, back-bonding from t_{2g} orbitals to the σ^* C−S bond is enhanced when the C−S bonds lie in the plane of the t_{2g} metal orbitals.[31] An analysis of the X-ray and calculated structures reveals that for $\mathbf{1}^{2+}$ (which incorporates the [12]aneS_4 ligand), some of the C−S bonds are in-plane and, as expected for such an interaction, a lengthening of these bonds is observed. However, in the structure of complex $\mathbf{3}^{2+}$ (which incorporates the [16]aneS_4 ligand) none of the C−S bonds are in-plane. These observations suggest that C−S σ^*/t_{2g} orbital overlap is *bigger* in $\mathbf{1}^{2+}$ than in $\mathbf{2}^{2+}$ and consequently $\mathbf{1}^{3+}$ would be the more localized structure. However, as mentioned previously, solid-state structures may be perturbed by packing interactions; furthermore, our previous studies have shown that [Ru([n]aneS_4)] structures can undergo considerable solution-phase dynamics.[14] In contrast, charge data obtained from the DFT studies are more consistent with the experimental data. The calculated ruthenium charges for $\mathbf{1}^{2+}$ are −0.600 and −0.602, while for $\mathbf{3}^{2+}$ the corresponding figures are −0.588 and −0.588. Although the difference is small these data suggest that the $\mathbf{1}^{2+}$ system is slightly more electron rich than the $\mathbf{3}^{2+}$.

Further research to address such unresolved questions and also address related, but more structurally complex functional oligonuclear systems based on the $[Ru^{II}Cl([n]aneS_3)]$ units deployed in this study will be discussed in future reports.

(31) (a) Mullen, G. E. D.; Went, M. J.; Wocaldo, S.; Powell, A. K.; Blower, P. J. *Angew. Chem., Int. Ed. Engl.* **1997**, *36*, 1205. (b) Mullen, G. E. D.; Fässler, T. F.; Went, M. J.; Howland, K.; Stein, B.; Blower, P. J. *J. Chem. Soc., Dalton Trans.* **1999**, 3759.

(32) Sutton, J. E.; Sutton, P. M.; Taube, H. *Inorg. Chem.* **1979**, *18*, 1017.

(33) Ribou, A.-C.; Launay, J.-P.; Takahashi, K.; Nihira, T.; Tarutani, S.; Spangler, C. W. *Inorg. Chem.* **1994**, *33*, 1325.

Experimental Section

Physical Measurements. Microanalyses for carbon, hydrogen, nitrogen, and sulfur were obtained using a Perkin-Elmer 2400 analyzer, working at 975 °C. ^{1}H NMR were recorded on a Bruker AM250 machine, working in Fourier transform mode. Spectra were acquired in the range 1−12 ppm with 32 K data points. Because of the presence of thiacrown-based invertomers (a previously reported phenomenon),[14] coupling constants cannot be quoted with accuracy; a full NMR analysis of this effect will form the basis of future reports. Mass spectra were obtained on a Kratos MS80 in positive ion mode with a *m*-nitrobenzyl alcohol matrix. UV/vis spectra were recorded on a Unicam UV/vis spectrometer UV2 in twin beam mode. Spectra were recorded in matched quartz cells and baseline corrected. CV was carried out using an EG&G Versastat II potentiostat and the Condecon 310 hardware/software package. Measurements were made using approximately 2×10^{-3} mol dm^{-3} solutions in dry solvents under a nitrogen atmosphere, with support electrolyte as stated. Potentials were measured with reference to a Ag/AgCl (saturated AgCl in saturated KCl) electrode. In the conditions used the ferrocene/ferrocenium couple was observed at 400 mV ($\Delta E_p = 60$ mV). UV/vis/NIR spectroelectrochemical measurements were performed in acetonitrile using an OTTLE cell thermostat at 273 K.

Syntheses. The ligand 6-bis(4-pyridyl)-1,2,4,5-tetrazine[34] and the complexes[Ru([12]aneS$_4$)(DMSO)Cl](PF$_6$),[Ru([14]aneS$_4$)(DMSO)-Cl](PF$_6$), and [Ru([16]aneS$_4$)(DMSO)Cl](PF$_6$) were synthesized by published procedures. All other chemicals were obtained from commercial sources and were used as supplied.

[{Ru([12]aneS$_4$)Cl}$_2$(μ-pyz)](PF$_6$)$_2$, [1](PF$_6$)$_3$. To a solution of 0.3 g (0.5 mmols) of [Ru([12]aneS$_4$)(DMSO)Cl](PF$_6$) in 20 mL of ethanol/water 1:1 was added pyrazine (0.02 g, 0.5 equiv), and the reaction mixture refluxed for 12 h. Excess NH_4PF_6 (0.2445 g, 3 equiv) was added to the warm solution, resulting in a red-orange precipitate which was quickly filtered and then washed with water and ethanol, then dried in vacuo. No further purification was needed. Mass = 0.087 g [**1**](PF$_6$)$_3$ (31%).^{1}H NMR (CD_3NO_2): δ_H = 2.9−3.6 (m, 32H), 8.7 (s, 4H). MS; *m*/*z* (%): 981 (63) [M$^+$ − PF$_6$]. $Ru_2C_{20}H_{36}N_2S_8Cl_2P_2F_{12}$ (1126): calcd C = 21.37%, H = 3.23%, S = 22.82%, N = 2.49%; found C = 20.85%, H = 3.48%, S = 22.27%, N = 2.74%.

[{Ru([14]aneS$_4$)Cl}$_2$(μ-pyz)](PF$_6$)$_2$, [2](PF$_6$)$_3$. To a solution of 0.3 g (0.478 mmols) of [Ru([14]aneS$_4$)(DMSO)Cl](PF$_6$) in 20 mL of ethanol/water 1:1 was added pyrazine (0.019 g, 0.5 equiv), and the reaction mixture refluxed for 12 h. Excess NH_4PF_6 (0.234 g, 3 equiv) was added to the warm solution, resulting in a red-orange precipitate which was quickly filtered and then washed with water and ethanol, then dried in vacuo. No further purification was needed. Mass = 0.102 g [**2**](PF$_6$) (36%).^{1}H NMR (CD_3NO_2): δ_H = 2.4−3.6 (m, 40H), 8.85 (s, 4H). MS; *m*/*z* (%):1035 (87) [M$^+$ − PF$_6$]. $Ru_2C_{24}H_{44}N_2S_8Cl_2P_2F_{12}$ (1182): calcd C =24.43%, H = 3.76%, S =21.74%, N = 2.37%; found C = 24.21%, H = 3.66%, S =22.13%, N = 2.59%.

[{Ru([16]aneS$_4$)Cl}$_2$(μ-pyz)](PF$_6$)$_2$, [3](PF$_6$)$_3$. To a solution of 0.3 g (0.457 mmols) of [Ru([16]aneS$_4$)(DMSO)Cl](PF$_6$) in 20 mL of ethanol/water 1:1 was added pyrazine (0.018 g, 0.5 equiv), and the reaction mixture refluxed for 12 h. Excess NH_4PF_6 (0.223 g, 3 equiv) was added to the warm solution, resulting in a red precipitate which was quickly filtered and then washed with water and ethanol, then dried in vacuo. No further purification was needed. Mass = 0.096 g [**3**](PF$_6$)$_2$ (34%).^{1}H NMR (CD_3NO_2): δ_H = 2.4−3.55 (m, 48H), 9.1 (s, 4H). MS; *m*/*z* (%): 1091 (100) [M$^+$ − PF$_6$], 946 (32) [M$^+$ − 2PF$_6$]. $Ru_2C_{28}H_{58}N_2S_8Cl_2O_3P_2F_{12}$ (**3**.3H$_2$O/1290): calcd C = 26.06%, H = 4.53%, S = 19.88%, N = 2.17%; found C = 26.13%, H = 4.41%, S = 20.01%, N = 2.37%.

[{Ru([12]aneS$_4$)Cl}$_2$(μ-4,4′-bpy)](PF$_6$)$_2$, [4](PF$_6$)$_3$. To a solution of 0.3 g (0.5 mmols) of [Ru([12]aneS$_4$)(DMSO)Cl](PF$_6$) in 20 mL of ethanol/water 1:1 was added 4,4′-bipyridine (0.039 g, 0.5 equiv), and the reaction mixture refluxed for 12 h. Excess NH_4PF_6 (0.2445 g, 3 equiv) was added to the warm solution, resulting in a yellow precipitate which was quickly filtered and then washed with water and ethanol, then dried in vacuo. No further purification was needed. Mass = 0.096 g [**4**](PF$_6$)$_2$ (32%).^{1}H NMR (CD_3NO_2): δ_H = 1.77−3.46 (m, 32H), 7.78 (d, 4H), 8.96(d, 4H). MS; *m*/*z* (%): 1057 (47) [M$^+$ − PF$_6$]. $Ru_2C_{26}H_{40}N_2S_8Cl_2P_2F_{12}$: calcd C = 26.02%, H = 3.33%, S = 21.33%, N = 2.33%; found C = 25.60%, H = 3.81%, S = 20.96%, N = 2.59%.

[{Ru([14]aneS$_4$)Cl}$_2$(μ-4,4′-bpy)](PF$_6$)$_2$, [5](PF$_6$)$_3$. To a solution of 0.3 g (0.478 mmols) of [Ru([14]aneS$_4$)(DMSO)Cl](PF$_6$) in 20 mL of ethanol/water 1:1 was added 4,4′-bipyridine (0.0373 g, 0.5 equiv), and the reaction mixture refluxed for 12 h. Excess NH_4PF_6 (0.234 g, 3 equiv) was added to the warm solution, resulting in a yellow precipitate which was quickly filtered and then washed with water and ethanol, then dried in vacuo. No further purification was needed. Mass = 0.089 g [**5**](PF$_6$)$_2$ 30(%).^{1}H NMR (CD_3NO_2): δ_H = 1.95−3.68 (m, 40H), 7.61 (d, 4H), 8.07(d, 4H). MS; *m*/*z* (%): 1113 (100) [M$^+$ − PF$_6$]. $Ru_2C_{30}H_{48}N_2S_8Cl_2P_2F_{12}$ (1258): calcd C =28.68%, H = 3.85%, S =20.42%, N = 2.23%; found C = 28.40%, H = 3.59%, S = 20.27%, N = 2.03%.

[{Ru([16]aneS$_4$)Cl}$_2$(μ-4,4′-bpy)](PF$_6$)$_2$, [6](PF$_6$)$_3$. To a solution of 0.3 g (0.457 mmols) of [Ru([16]aneS$_4$)(DMSO)Cl](PF$_6$) in 20 mL of ethanol/water 1:1 was added 4,4′-bipyridine (0.0357 g, 0.5 equiv), and the reaction mixture refluxed for 12 h. Excess NH_4PF_6 (0.223 g, 3 equiv) was added to the warm solution, resulting in a yellow precipitate which was quickly filtered and then washed with water and ethanol, then dried in vacuo. No further purification was needed. Mass = 0.096 g [**6**](PF$_6$)$_2$ (32%).^{1}H NMR (CD_3NO_2): δ_H =1.86−3.46 (m, 48H), 7.91 (d, 4H), 9.07(d, 4H). MS; *m*/*z* (%): 1169 (100) [M$^+$ − PF$_6$]. $Ru_2C_{34}H_{56}N_2S_8Cl_2P_2F_{12}$ (1314): calcd C = 31.12%, H = 4.30%, S = 19.55%, N = 2.13%; found C = 30.73%, H = 4.11%, S = 19.68%, N = 2.49%.

[{Ru([12]aneS$_4$)Cl}$_2$(μ-4-bptz)](PF$_6$)$_2$, [7](PF$_6$)$_3$. To a solution of 0.3 g (0.5 mmols) of [Ru([12]aneS$_4$)(DMSO)Cl](PF$_6$) in 20 mL of ethanol/water 1:1, was added 3,6-bis(4-pyridyl)-1,2,4,5-tetrazine (0.059 g, 0.5 equiv), and the reaction mixture refluxed for 12 h. Excess NH_4PF_6 (0.2445 g, 3 equiv) was added to the warm solution, resulting in a yellow precipitate which was quickly filtered and then washed with water and ethanol, then dried in vacuo. No further purification was needed. Mass = 0.093 g [**7**](PF$_6$)$_2$ (29%). ^{1}H NMR (CD_3NO_2): δ_H = 2.35−3.72 (m, 32H), 7.62−8.94 (m, 8H). MS; *m*/*z* (%): 1137 (100) [M$^+$ − PF$_6$]. $Ru_2C_{28}H_{40}N_6S_8Cl_2P_2F_{12}$: calcd C = 26.27%, H = 3.15%, S = 20.04%, N = 6.56%; found C = 25.44%, H = 3.50%, S = 20.31%, N = 6.66%.

[{Ru([14]aneS$_4$)Cl}$_2$(μ-4-bptz)](PF$_6$)$_2$, [8](PF$_6$)$_3$. To a solution of 0.3 g (0.478 mmols) of [Ru([14]aneS$_4$)(DMSO)Cl](PF$_6$) in 20 mL of ethanol/water 1:1 was added 3,6-bis(4-pyridyl)-1,2,4,5-tetrazine (0.056 g, 0.5 equiv), and the reaction mixture refluxed for 12 h. Excess NH_4PF_6 (0.234 g, 3 equiv) was added to the warm solution, resulting in a yellow precipitate which was quickly filtered and then washed with water and ethanol, then dried in vacuo. No further purification was needed. Mass = 0.109 g [**8**](PF$_6$)$_2$ (34%).^{1}H NMR (CD_3NO_2): δ_H = 1.78−3.92 (m, 40H), 7.43−9.07 (m, 8H).

(34) Forster, R. J.; Keyes, T. E.; Bond, A. M. *J. Phys. Chem. B* **2000**, *104*, 6389.

MS; *m*/*z* (%): 1193 [$M^+ - PF_6$]. $Ru_2C_{32}H_{48}N_6S_8Cl_2P_2F_{12}$: calcd C = 28.76%, H = 3.62%, S = 19.19%, N = 6.29%; found C = 28.52%, H = 3.89%, S = 19.19%, N = 6.09%.

[{Ru([16]aneS$_4$)Cl}$_2$(μ-4-bptz)](PF$_6$)$_2$, [9](PF$_6$)$_3$. To a solution of 0.3 g (0.457 mmols) of [Ru([16]aneS$_4$)(DMSO)Cl](PF$_6$) in 20 mL of ethanol/water 1:1 was added 3,6-bis(4-pyridyl)-1,2,4,5-tetrazine (0.054 g, 0.5 equiv), and the reaction mixture refluxed for 12 h. Excess NH_4PF_6 (0.223 g, 3 equiv) was added to the warm solution, resulting in a precipitate which was quickly filtered and then washed with water and ethanol, then dried in vacuo. No further purification was needed. Mass = 0.118 g [**9**](PF$_6$)$_2$ (37%).^{1}H NMR (CD_3NO_2): δ_H = 1.95−3.68 (m, 48H), 7.61−9.22 (m, 8H). MS; *m*/*z* (%): 1249 (78) [$M^+ - PF_6$]. $Ru_2C_{36}H_{56}N_6S_8Cl_2P_2F_{12}$: calcd C = 31.06%, H = 4.05%, S = 18.42%, N = 6.04%; found C = 31.45%, H = 3.60%, S = 18.31%, N = 6.37%.

Crystal Structure Determinations. Crystals of [**1**][(PF$_6$)$_2$], and [**6**][(PF$_6$)$_2$] were grown by vapor diffusion of diethyl ether into nitromethane solutions, while [**3**][(PF$_6$)$_2$] was grown by vapor diffusion of diethyl ether into an acetone solution. Relevant crystallographic data are summarized in Supporting Information, Table S6. In all three cases, data was collected at 150 K on a Bruker Smart CCD area detector with Oxford Cryosystems low temperature system, and complex scattering factors were taken from the program package SHELXTL[35] as implemented on the Viglen Pentium computer. Hydrogen atoms were placed geometrically and refined with a riding model and with U_{iso} constrained to be 1.2 times U_{eq} of the carrier atom. Molecular diagrams were drawn with PLATON.[36]

CCDC 684573−68475 contain the supplementary crystallographic data for this paper. These data can be obtained free of charge on application to CCDC, 12 Union Road, Cambridge CB21EZ, U.K. (fax: (á44) 1223−336−033; e-mail: deposit@ccdc.cam.ac.uk).

DFT Calculations. Density Functional Theory (DFT)[37] calculations were performed using the Gaussian 03 package.[38] Geometry optimizations were performed without any constraints using the hybrid B3LYP method. This functional includes a mixture of Hartree−Fock[39] exchange with DFT[37] exchange-correlation, given by Becke's three-parameter functional[40] with the Lee, Yang, and Parr correlation functional, which includes both local and nonlocal terms.[41] The standard Stuttgart/Dresden (SDD) basis set along with the associated ECP[42] was used for the Ru while the standard 6−31G* basis set was used for the remaining elements.[43] Spin unrestricted calculations were performed for the paramagnetic species. TD-DFT calculations were also performed using the Gaussian 03 implementation[44] on the B3LYP-optimized structures.

Acknowledgment. P.J.C. thanks FCT for a postdoctoral grant (SFRH/BPD/27082/2006). M.N. is grateful for an EPSRC PhD studentship.

Supporting Information Available: Table S1 containing the optimized distances of complexes **1**$^{2+}$, **3**$^{2+}$, and **6**$^{2+}$ and respective oxidized forms; Tables S2−S4 with the atomic/fragment contributions (%) to the molecular orbitals of the studied complexes; Table S5 contains the crystal data and pertinent refinement details for dinuclear complexes ^{1}(PF$_6$)$_2$, [**3**](PF$_6$)$_2$and [**6**](PF$_6$)$_2$. This material is available free of charge via the Internet at http://pubs.acs.org.

IC801193R

(35) *SHELXTL, An integrated system for solving and refining crystal structures from diffraction data*, Revision 5.1; Bruker AXS Ltd.: Madison, WI.
(36) Spek, A. L. *J. Appl. Crystallogr.* **2003**, *36*, 7–13.
(37) Parr, R. G.; Yang, W. *Density Functional Theory of Atoms and Molecules*; Oxford University Press: New York, 1989.
(38) Frisch, M. J.; Trucks, G. W.; Schlegel, H. B.; Scuseria, G. E.; Robb, M. A.; Cheeseman, J. R.; Zakrzewski, V. G.; Montgomery, J. A., Jr.; Stratmann, R. E.; Burant, J. C.; Dapprich, S.; Millam, J. M.; Daniels, A. D.; Kudin, K. N.; Strain, M. C.; Farkas, O.; Tomasi, J.; Barone, V.; Cossi, M.; Cammi, R.; Mennucci, B.; Pomelli, C.; Adamo, C.; Clifford, S.; Ochterski, J.; Petersson, G. A.; Ayala, P. Y.; Cui, Q.; Morokuma, K.; Rega, N.; Salvador, P.; Dannenberg, J. J.; Malick, D. K.; Rabuck, A. D.; Raghavachari, K.; Foresman, J. B.; Cioslowski, J.; Ortiz, J. V.; Baboul, A. G.; Stefanov, B. B.; Liu, G.; Liashenko, A.; Piskorz, P.; Komaromi, I.; Gomperts, R.; Martin, R. L.; Fox, D. J.; Keith, T.; Al-Laham, M. A.; Peng, C. Y.; Nanayakkara, A.; Challacombe, M.; Gill, P. M. W.; Johnson, B.; Chen, W.; Wong, M. W.; Andres, J. L.; Gonzalez, C.; Head-Gordon, M.; Replogle, E. S.; Pople, J. A. *Gaussian 03*, revision B.04; Gaussian, Inc.: Wallingford, CT, 2004.
(39) Hehre, W. J.; Radom, L.; Schleyer, P. v. R.; Pople, J. A. *Ab Initio Molecular Orbital Theory*; Wiley: New York, 1986.
(40) Becke, A. D. *J. Chem. Phys.* **1993**, *98*, 5648.
(41) Lee, C.; Yang, W.; Parr, R. G. *Phys. Rev. B* **1988**, *37*, 785.
(42) Andrae, D.; Hauessermann, U.; Dolg, M.; Stoll, H.; Preuss, H. *Theor. Chim. Acta* **1990**, *77*, 123–141.
(43) (a) Ditchfield, R.; Hehre, W. J.; Pople, J. A. *J. Chem. Phys.* **1971**, *54*, 724. (b) Hehre, W. J.; Ditchfield, J. A.; Pople, J. A. *J. Chem. Phys.* **1972**, *56*, 2257. (c) Hariharan, P. C.; Pople, J. A. *Theor. Chim. Acta* **1973**, *28*, 213. (d) Hariharan, P. C.; Pople, J. A. *Mol. Phys.* **1974**, *27*, 209. (e) Gordon, M. S. *Chem. Phys. Lett.* **1980**, *76*, 163.
(44) (a) Stratmann, R. E.; Scuseria, G. E.; Frisch, M. J. *J. Chem. Phys.* **1998**, *109*, 8218. (b) Bauernschmitt, R.; Ahlrichs, R. *Chem. Phys. Lett.* **1996**, *256*, 454. (c) Casida, M. E.; Jamorski, C.; Casida, K. C.; Salahub, D. R. *J. Chem. Phys.* **1998**, *108*, 4439.